Improvement of electrocatalytic water oxidation activity of novel copper complex by modulating axial coordination of phosphate on metal center

Jieying Wang,‡[a] Yezi Ping,‡[a] Yanmei Chen,[a] Shanshan Liu,[a] Jinfeng Dong,[a] Zhijun Ruan,*[a] Xiangming Liang,*[b] Junqi Lin*[a]

[a] Hubei Key Laboratory of Processing and Application of Catalytic Materials, College of Chemistry and Chemical Engineering, Huanggang Normal University, Huanggang 438000, China.

E-mail: ruanzhijun@hgnu.edu.cn; linjunqi@hgnu.edu.cn

[b] School of Basic Medical Sciences, Ningxia Medical University, Yinchuan 750004, China.

E-mail: liangxm@nxmu.edu.cn

‡ These authors contributed equally to this work.

Synthesis of the bipyridine-based ligand 6,6′-bis(dimethylaminomethyl)-2,2′-bipyridine (dmabpy) and 6,6′-bis(methylaminomethyl)-2,2′-bipyridine (mabpy)

6,6′-Bis(bromomethyl)-2,2′-bipyridine: A mixture of N-bromosuccinimide (NBS, 4.00 g, 22.4 mmol) and 6,6′-dimethyl-2,2′-bipyridine (2.00 g, 10.84 mmol) in $CHCl_3$ (60 ml) was heated to 62 °C for half an hour. After the addition of catalytic benzoyl peroxide (800 mg, 3.30 mmol), the solution was refluxed at 62 °C for 16 h, cooled to room temperature and the solvent was removed. The yellow residue was triturated with MeOH (5 × 15 ml) and the white solid was recrystallized from chloroform to give the product as a white crystalline solid (0.385 g, 20.0 %).

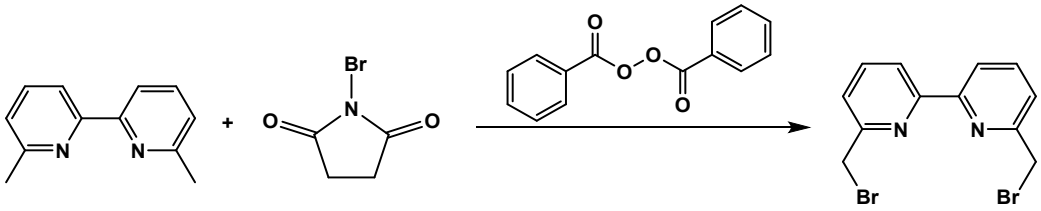

Scheme S1 The synthesis procedure of precursor 6,6′-Bis(bromomethyl)-2,2′-bipyridine.

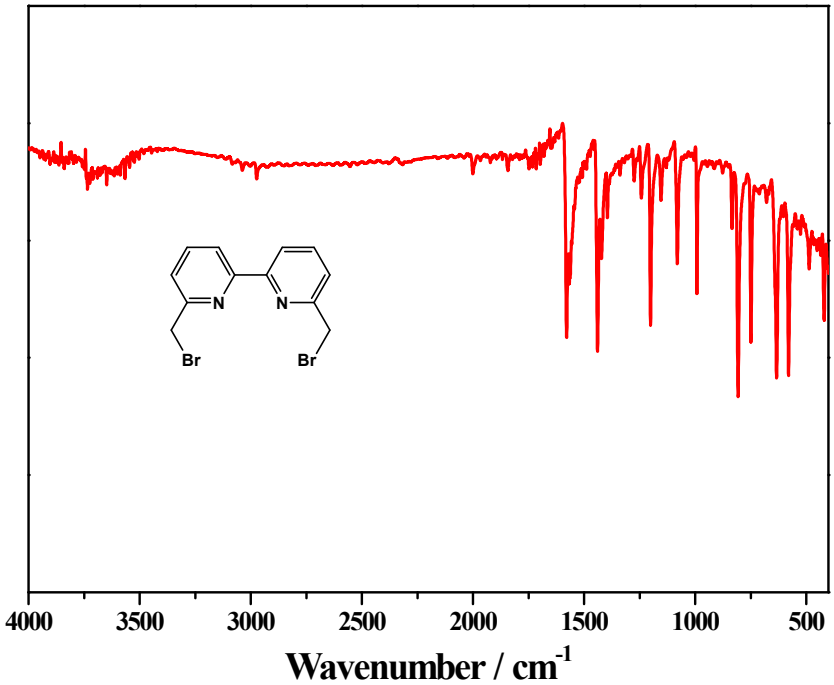

Fig. S1 FT-IR spectrum of precursor 6,6′-Bis(bromomethyl)-2,2′-bipyridine.

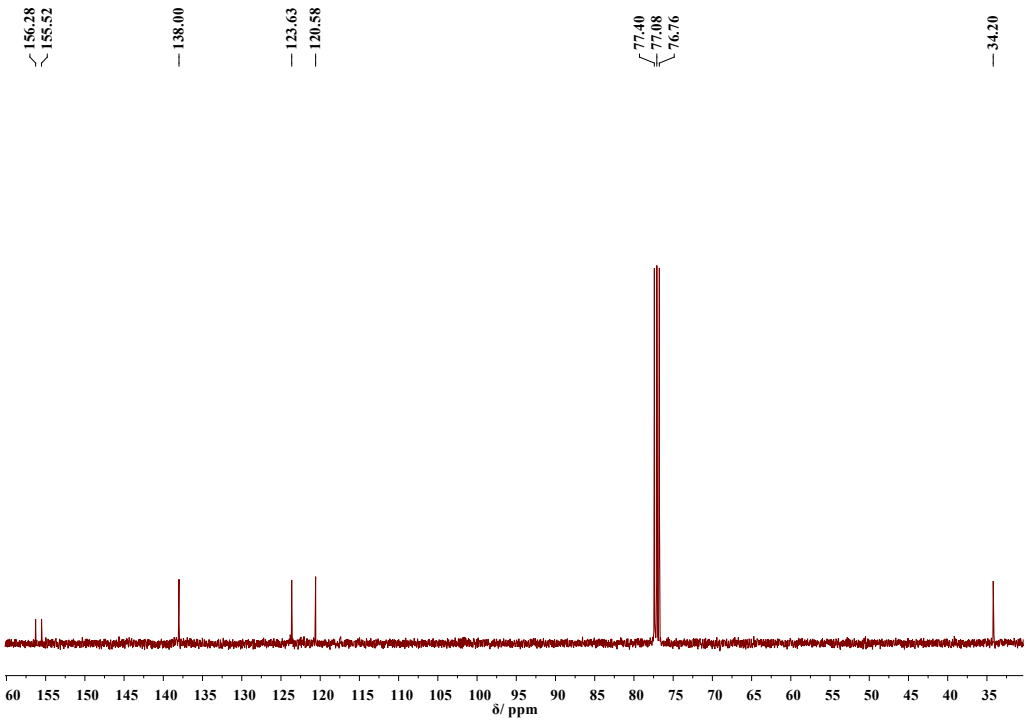

Fig. S2 The ^{13}C NMR (Bruker Avance III 400 MHz, chloroform-*d*) of 6,6′-Bis(bromomethyl)-2,2′-bipyridine: δ 156.2 (C_{py}), 155.5 (C_{py}), 138.0 (C_{py}), 123.7 (C_{py}), 120.6 (C_{py}), 34.2 (CH_2).

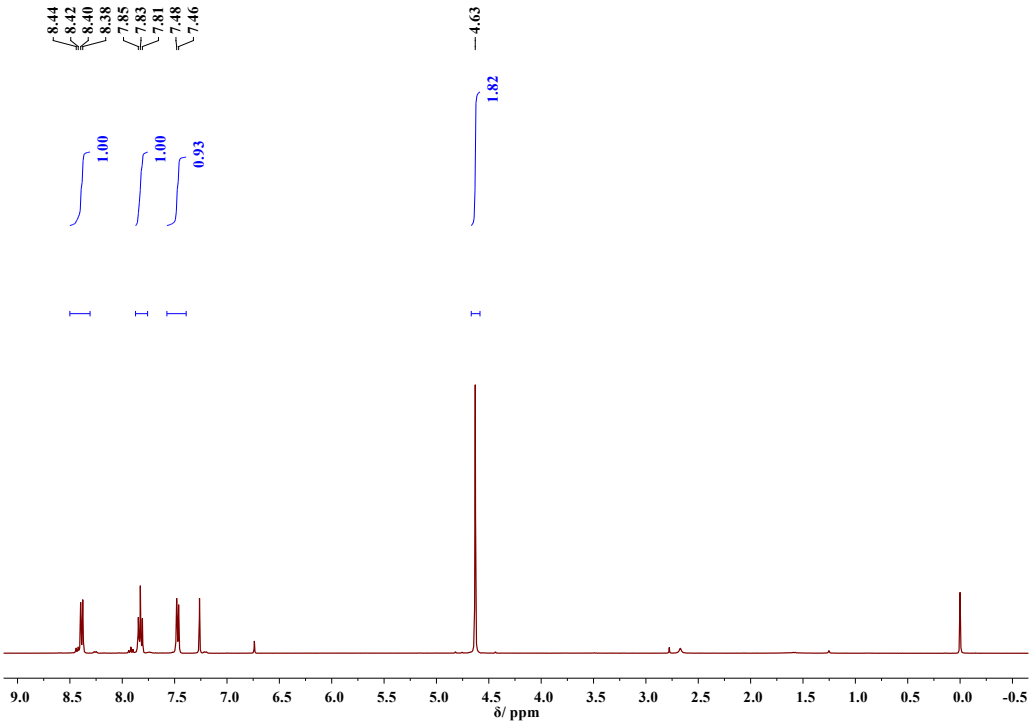

Fig. S3 The ^{1}H NMR (Bruker Avance III 400 MHz, chloroform-*d*) of 6,6′-Bis(bromomethyl)-2,2′-bipyridine: δ 8.40 (dd, J_{HH} = 7.8 Hz, J_{HH} = 1.0 Hz, 2H, CH_{py}), 7.84 (t, J_{HH} = 7.8 Hz, 2H, CH_{py}), 7.47 (dd, $^{3}J_{HH}$ = 7.8, J_{HH} = 1.0 Hz, 2H, CH_{py}), 4.64 (s, 4H, CH_2).

dmabpy: 6,6′-bis(bromomethyl)-2,2′-bipyridyl (0.268 g, 0.784 mmol) was dissolved in ethanol (10 mL). A 40% (w/w) aqueous solution of dimethylamine (4.0 ml, 8.0 mmol) was added dropwise. The mixture was refluxed at 80 °C for 16 h and then cooled to room temperature, the solvent was removed under reduced pressure. To deprotonate the compound, the white residue was dissolved in aqueous solution of NaOH (3 M, 10 ml). The solution was extracted with CH_2Cl_2 (3 × 10 ml). The organic layers were combined, dried under anhydrous sodium sulfate and the solvent was removed under reduced pressure. The residue was dried under high vacuum and the dmabpy ligand was obtained as bright yellow solid (0.20 g, 94.3 %).

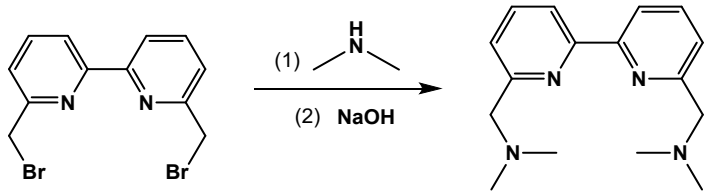

Scheme S2 The synthesis procedure of the ligand dmabpy.

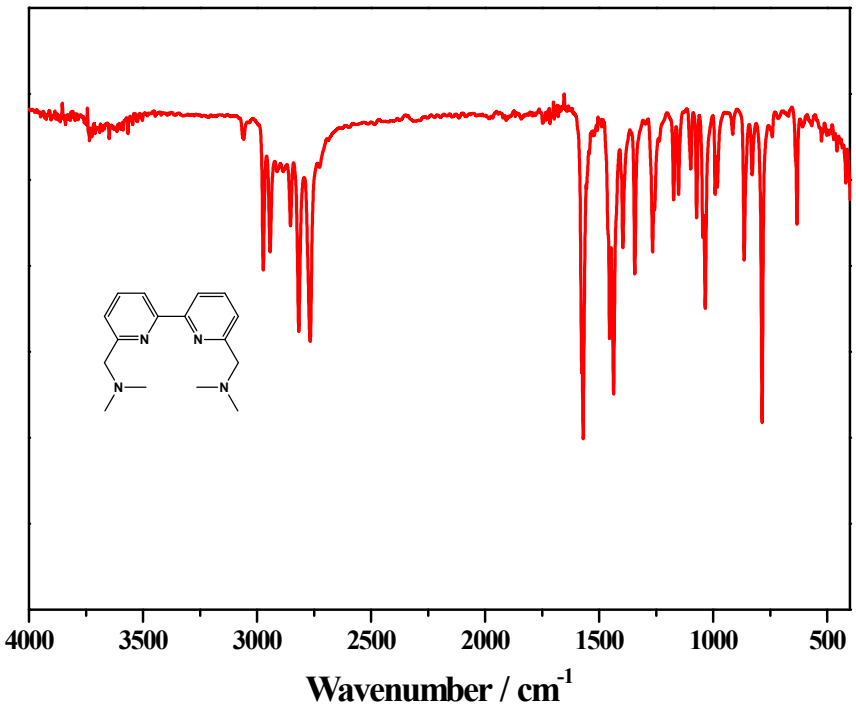

Fig. S4 FT-IR spectrum of the ligand dmabpy.

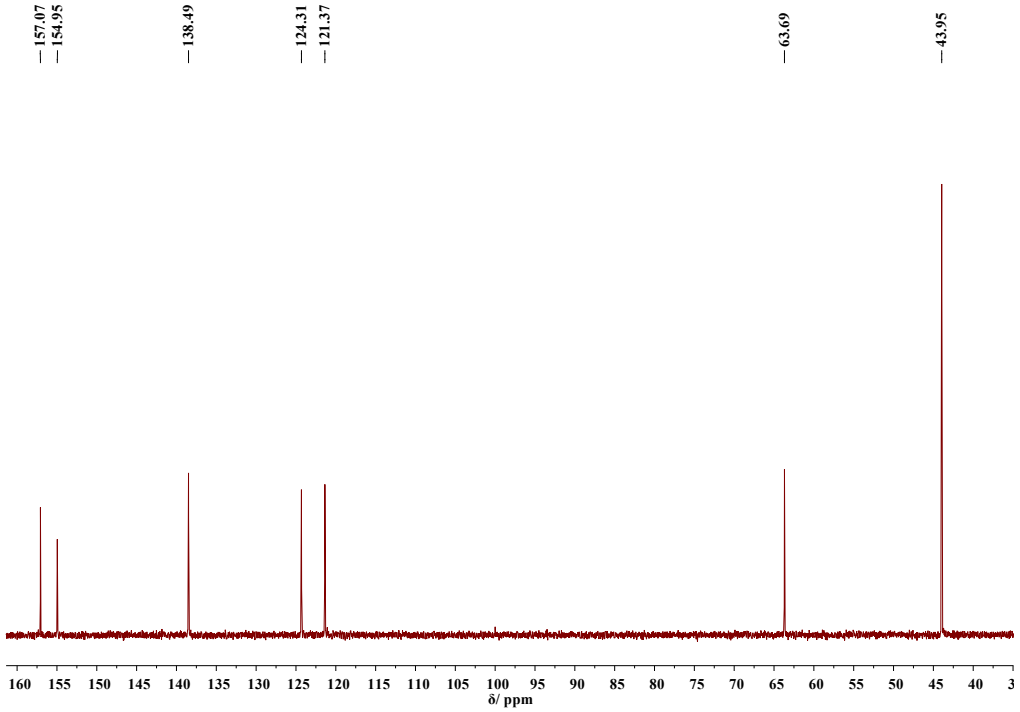

Fig. S5 ^{13}C NMR (Bruker Avance III 400 MHz, deuterium oxide) of dmabpy: δ 157.1 (C_{py}), 155.0 (C_{py}), 138.5 (C_{py}), 124.3 (C_{py}), 121.4 (C_{py}), 63.7 (CH_2), 44.0 (CH_3).

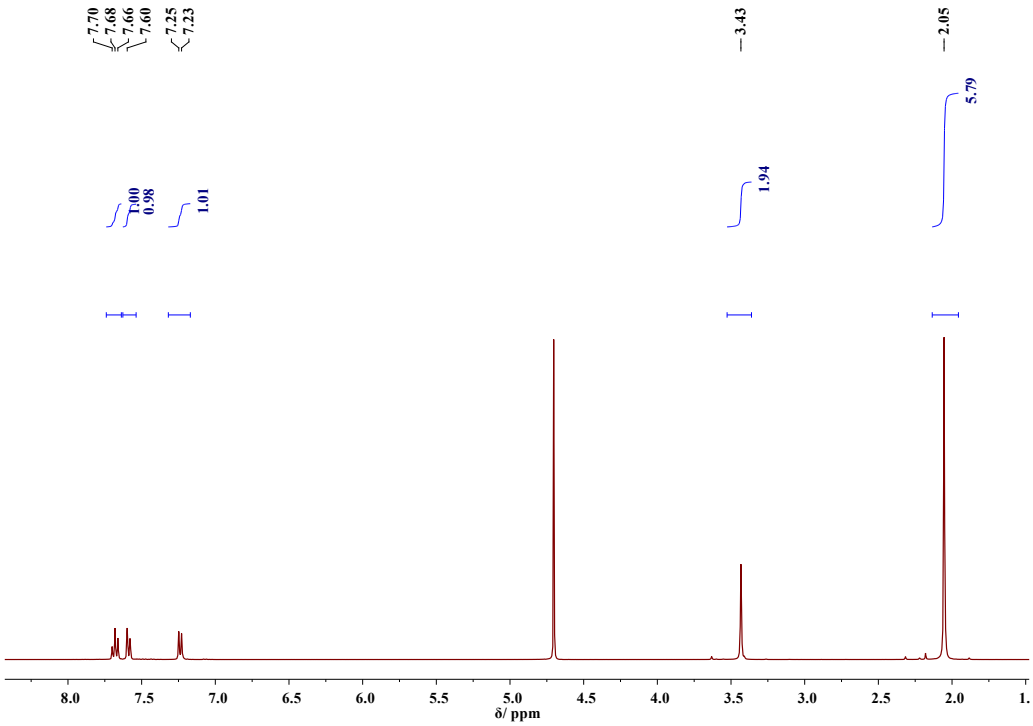

Fig. S6 The ^{1}H NMR (Bruker Avance III 400 MHz, deuterium oxide) of dmabpy: δ 7.76 (dd, J_{HH} = 7.9, J_{HH} = 3.3 Hz, 2H, CH_{py}), 7.60 (t, J_{HH} = 7.9 Hz, 2H, CH_{py}), 7.24 (dd, J_{HH} = 7.9, J_{HH} = 3.3 Hz, 2H, CH_{py}), 3.43 (s, 4H, CH_2), 2.05 (s, 12H, CH_3).

mabpy: The ligand mabpy was synthesized according to a similar preparation procedure as that of ligand dmabpy except that aqueous solution of methylamine was used instead of aqueous solution of dimethylamine. Ligand mabpy was formed as yellow oil (0.142 g, 75 %).

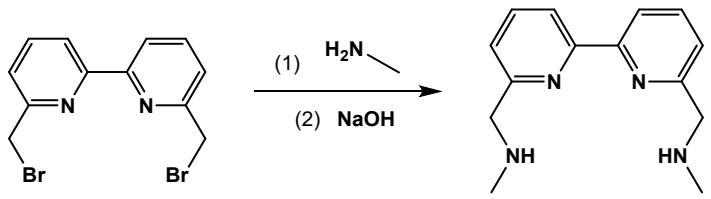

Scheme S3 The synthesis procedure of the ligand mabpy.

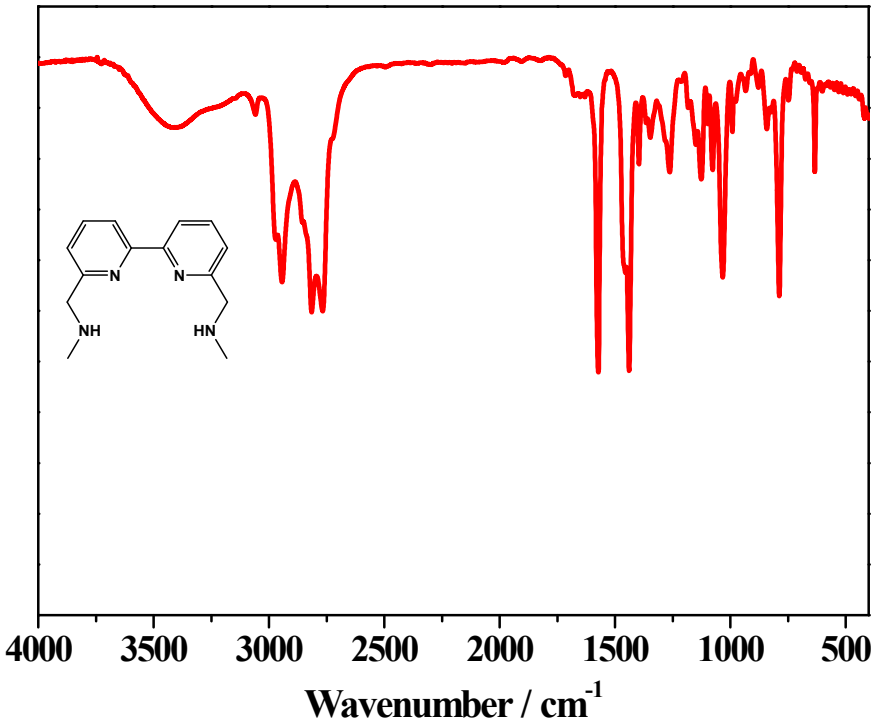

Fig. S7 FT-IR spectrum of the ligand mabpy.

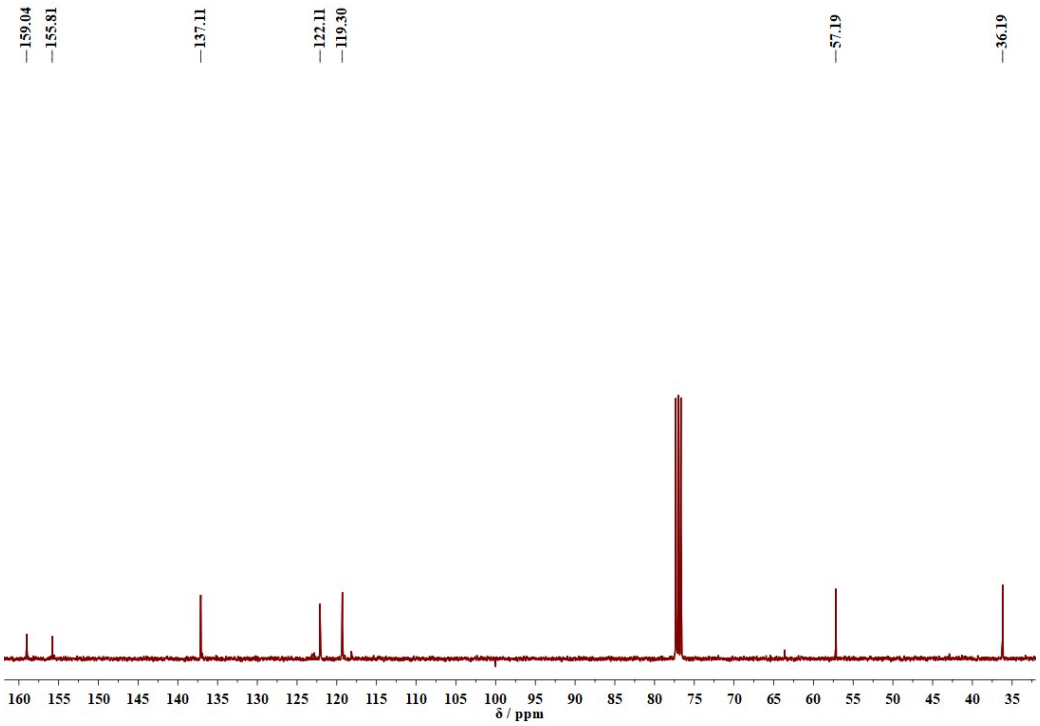

Fig. S8 ^{13}C NMR (Bruker Avance III 400 MHz, chloroform-*d*) of mabpy: δ 159.0 (C_{py}), 155.8 (C_{py}), 137.1 (C_{py}), 122.1 (C_{py}), 119.3 (C_{py}), 57.2 (CH_2), 36.2 (CH_3).

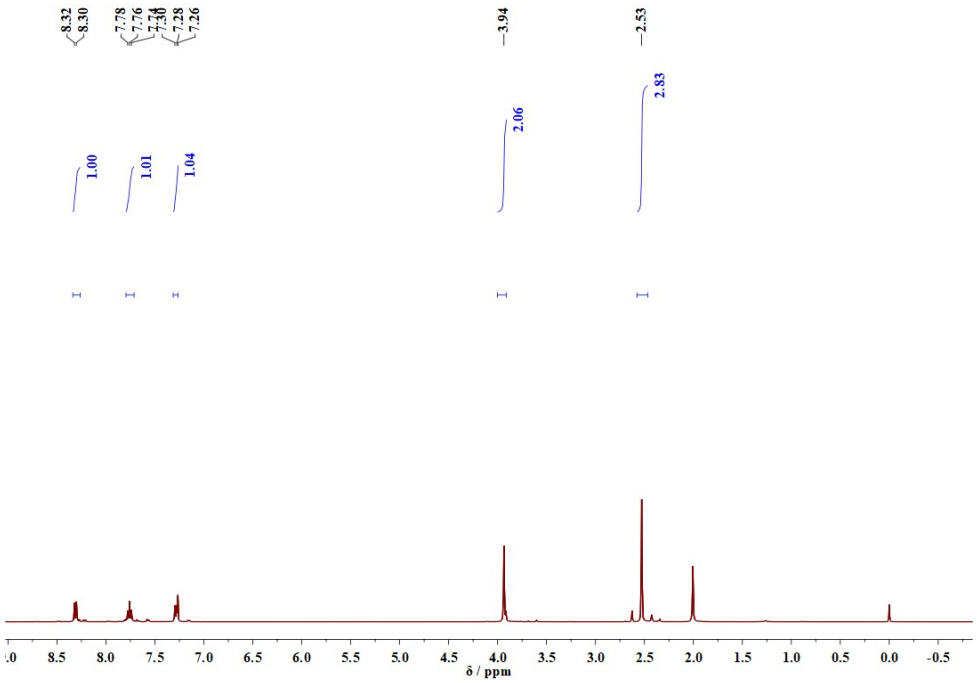

Fig. S9 The ^{1}H NMR (Bruker Avance III 400 MHz, chloroform-*d*) of mabpy: δ 8.31 (d, J_{HH} = 7.8 Hz, 2H, CH_{py}), 7.84 (t, J_{HH} = 7.7 Hz, 2H, CH_{py}), 7.47 (m, 2H, CH_{py}), 3.94 (s, 4H, CH_2), 2.53 (s, 6H, CH_2), 2.01 (s, NH).

Table S1 Crystallographic data and processing parameters for complexes **1**

Complex parameters	Complex **1**
Empirical formula	$C_{16}H_{22}Cl_2N_4CuO_8$
Formula weight	532.81
Temperature / K	192.0
Wavelength / Å	0.71073
Crystal system	Orthorhombic
Space group	Pnma
a / Å	13.3806(4)
b / Å	11.9359(4)
c / Å	12.9332(5)
α / deg	90
β / deg	90
γ / deg	90
Volume / Å^3	2065.55(12)
Z	4
Calculated density / Mg m^3	1.713
Absorption coefficient / mm^{-1}	1.370
F(000)	1092
Crystal size / mm^3	0.210 × 0.190 × 0.180
θ range / deg	2.190 to 26.388
Index ranges	-16≤h≤16 -14≤h≤14 -16≤h≤16
Reflections collected	43215
Independent reflections	2218 [*R*(int) = 0.0793]
Completeness to theta	99.9 % (25.099°)
Refinement method	Full-matrix least-squares on F^2
Data / restraints / parameters	2218 / 7 / 153
Goodness-of-fit on F^2	1.039
Final R indices [I>2sigma(I)]	R_1 = 0.0287, wR_2 = 0.0728
R indices (all data)	R_1 = 0.0334, wR_2 = 0.0761
Largest diff. peak and hole	1.673 and -1.747 e.Å^{-3}

$R_1 = \Sigma||F_o| - |F_c||/\Sigma|F_o|$, $wR_2 = [\Sigma(|F_o|^2 - |F_c|^2)^2/\Sigma(F_{o2})]^{1/2}$

Table S2 Selected bond lengths (Å) and angles (deg) for complexes **1**

Complex	**1**
Bond length (Å)	
Cu1–N1	2.054(2)
Cu1–N2	1.942(2)
Cu1–N3	1.942(2)
Cu1–N4	2.054(2)
Bond angles (deg)	
N1–Cu1–N2	82.25(8)
N2–Cu1–N3	79.29(10)
N3–Cu1–N4	82.25(8)
N1–Cu1–N4	113.16(12)

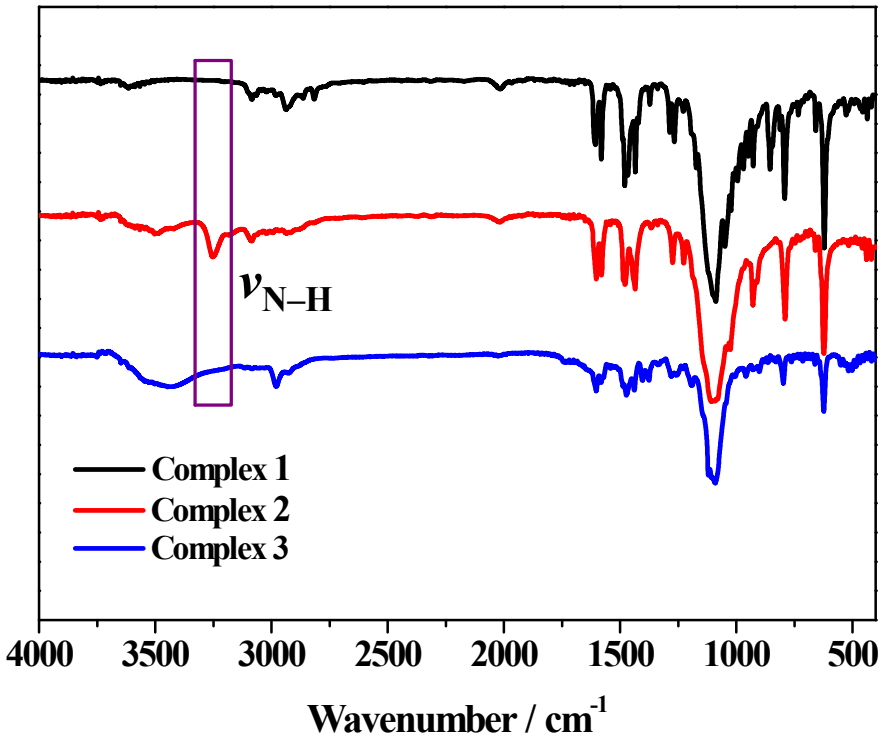

Fig. S10 FT-IR spectra of complex [Cu(dmabpy)]$(ClO_4)_2$ (**1**), complex [Cu(mabpy)]$(ClO_4)_2$ (**2**) and [Cu(*t*-bmabpy)]$(ClO_4)_2$ (**3**).

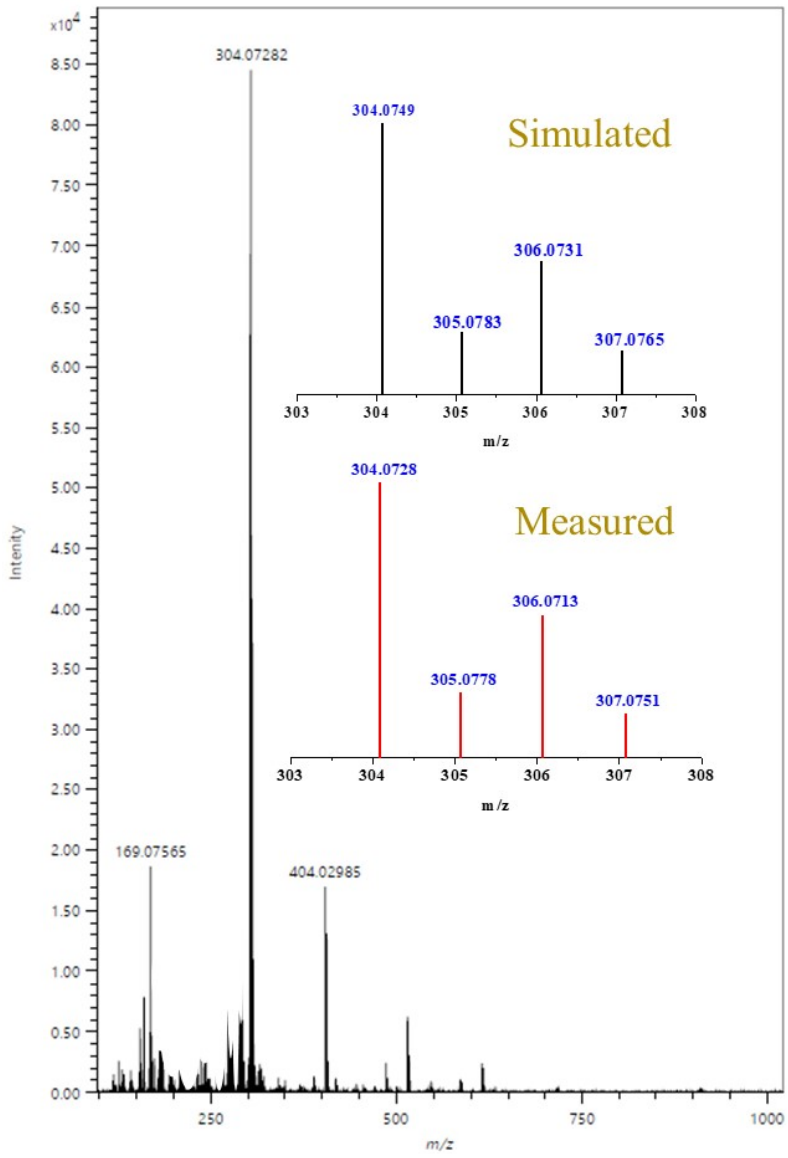

Fig. S11 The measured and simulated high resolution mass spectrum peak of the fragment of $[Cu(mabpy)\text{-}H^+]^+$ from complex **2** dissolved in water.

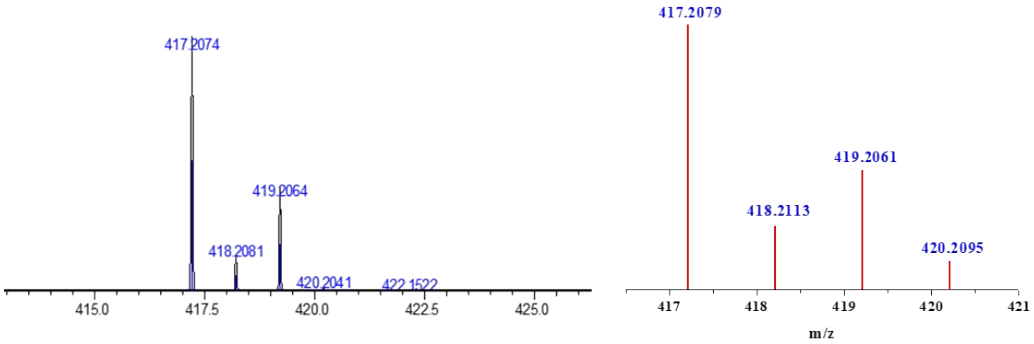

Fig. S12 The measured (left) and simulated (right) high resolution mass spectrum peak the fragment of $[Cu(t\text{-}bmabpy)]^+$ from complex **3** dissolved in water.

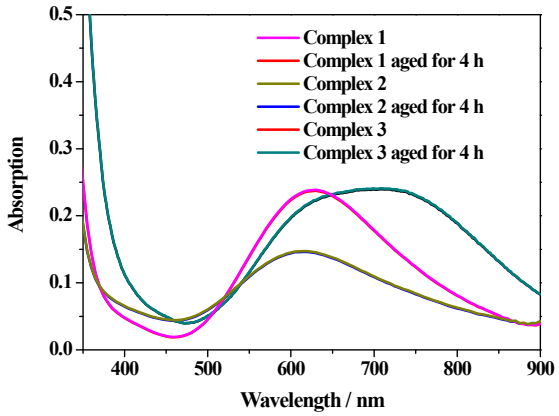

Fig. S13 UV-vis absorption of 1 mM of **1** and **2** in 0.1 M phosphate buffer solution at pH 9.0.

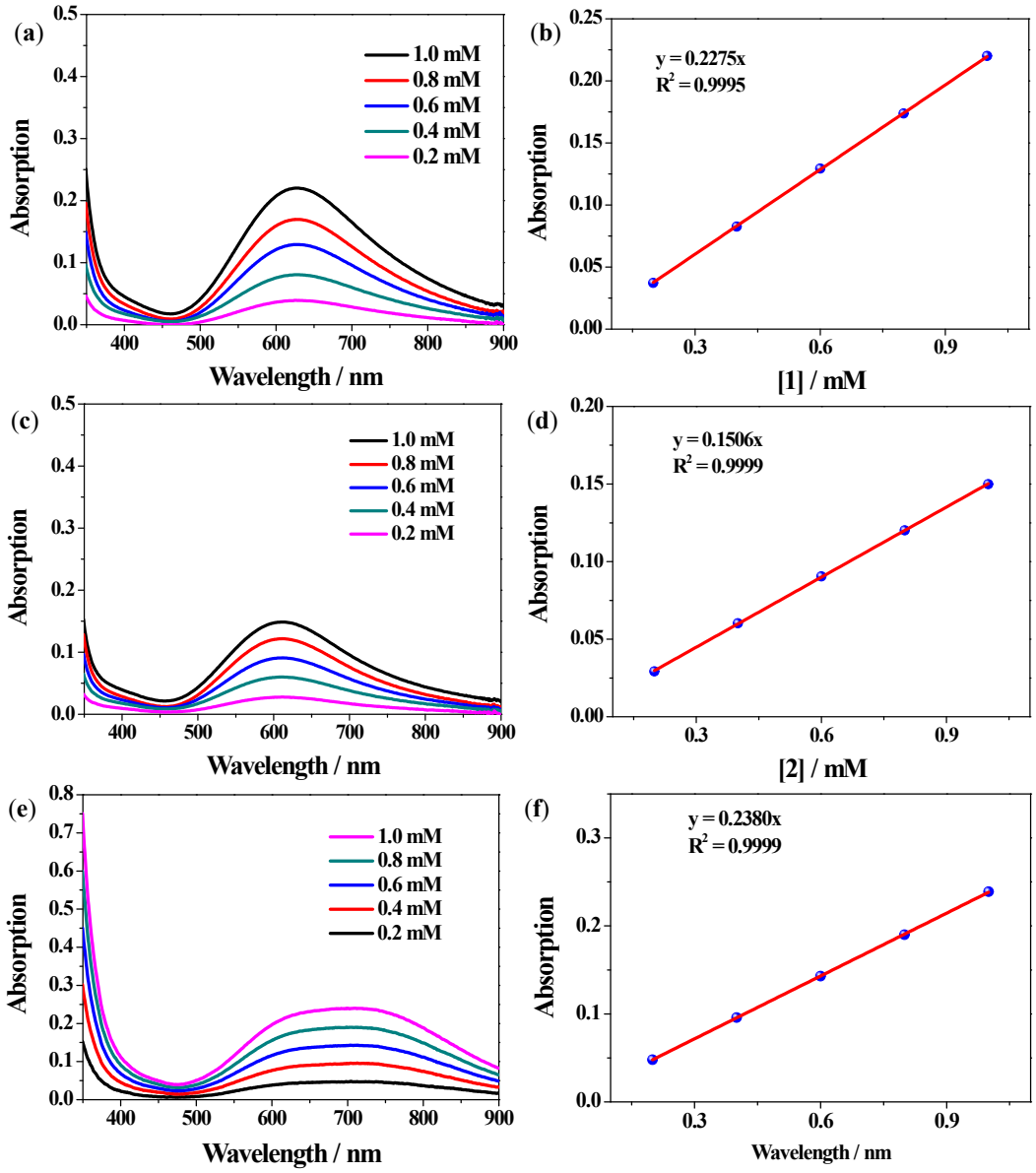

Fig. S14 Concentration -dependent UV-vis absorption spectra of **1** (a and b), **2** (c and d) and **3** (e and f) in PBS at pH 9.0.

Table S3 The UV-vis absorption properties of complexes **1**, **2** and **3**.

Complex	λ_{max} / nm	ε/ M^{-1} cm^{-1}
1	627	227.5
2	611	150.6
3	704	238.0

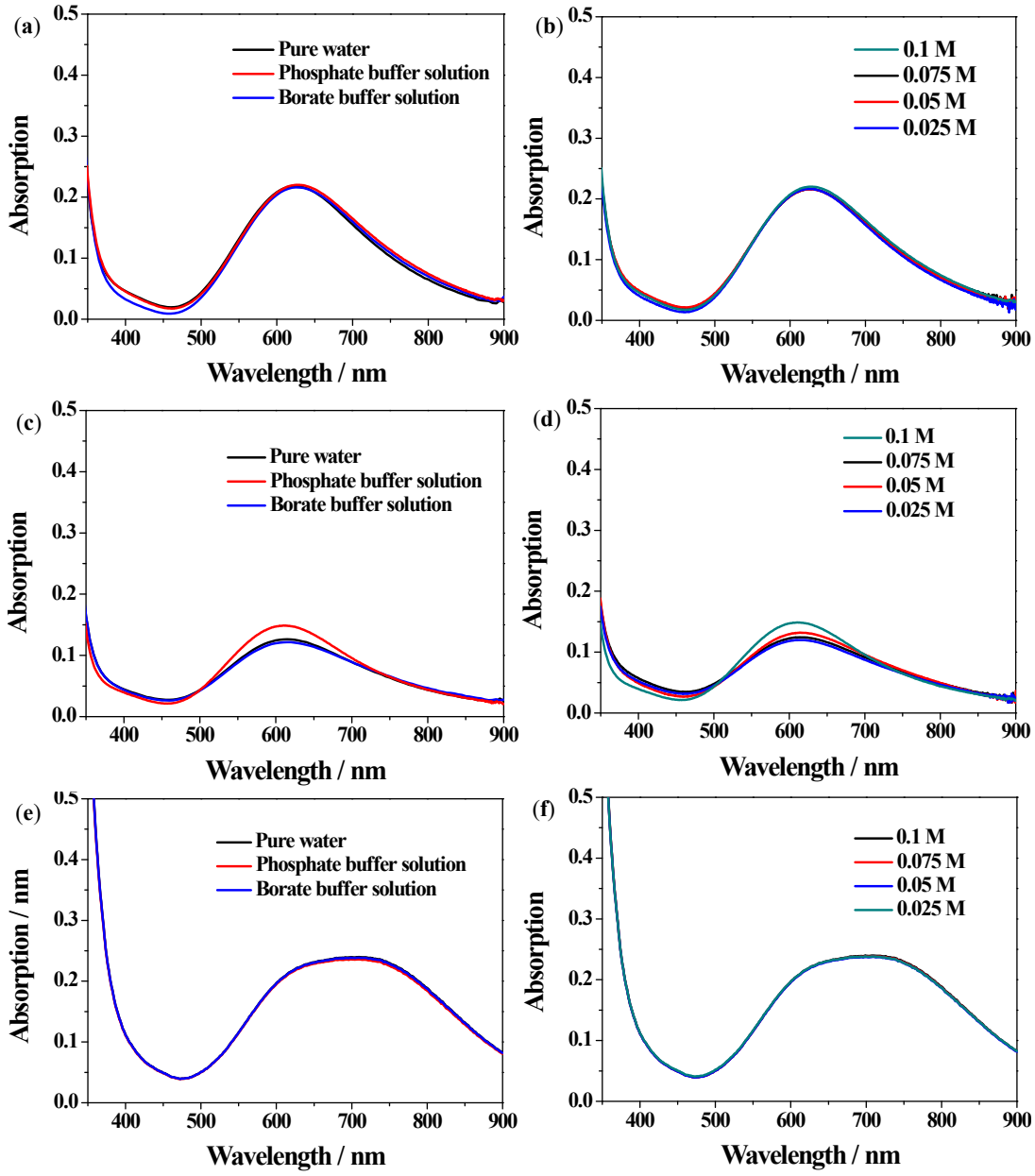

Fig. S15 UV-vis absorption spectra of 1 mM of complex **1** (a and b), **2** (c and d) and **3** (e and f) in pure water and 0.1 M different buffer solution at pH 9.0, and in PBS of various concentration at pH 9.0.

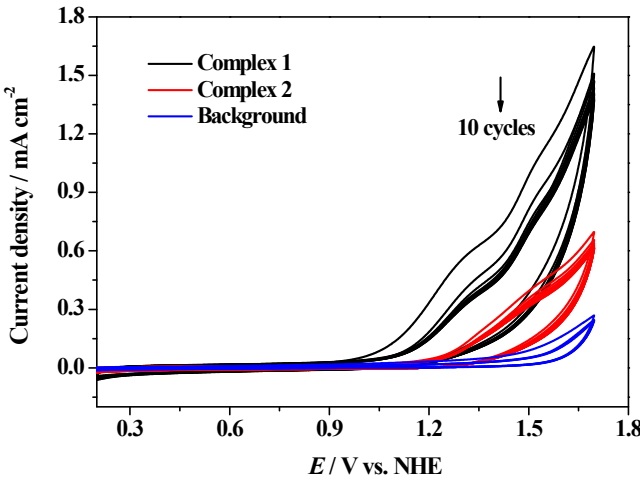

Fig. S16 Consecutive CV cyclic scan curves of 1 mM of complexes **1** and **2** in 0.1 M PBS at pH 9.0, scan rate = 100 mV/s.

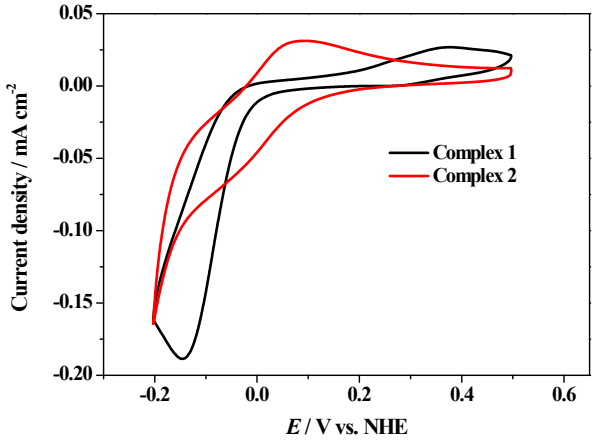

Fig. S17 The Cu^{I}/Cu^{II} couple of complex **1** and **2** in 0.1 M PBS at pH 9.0, scan rate = 100 mV/s.

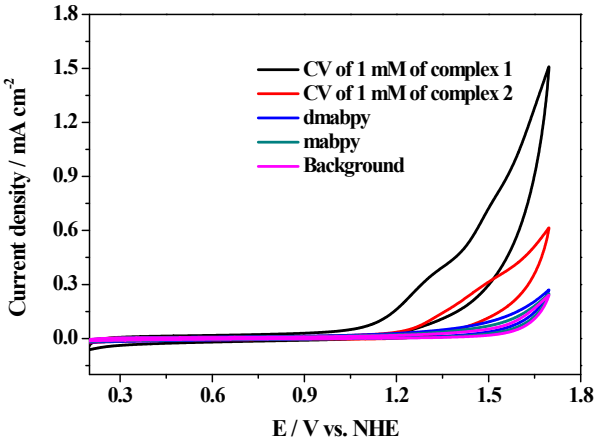

Fig. S18 CV tests and rinse tests of 1 mM of complexes 1, 2, ligand dmabpy and mabpy in 0.1 M PBS at pH 9.0, scan rate = 100 mV s−1, GC electrode was used as the working electrode.

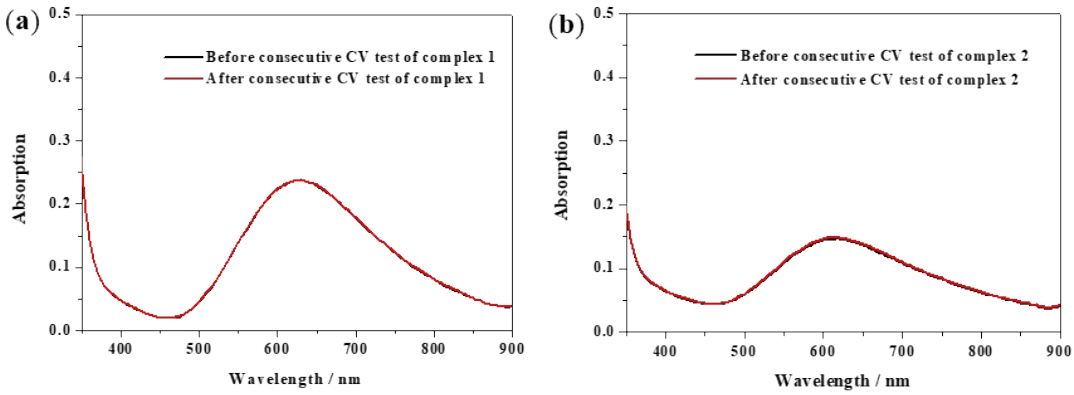

Fig. S19 The UV-vis absorption spectra of the electrolyte containing complex **1** (a) and **2** (b) before and after consecutive CV test.

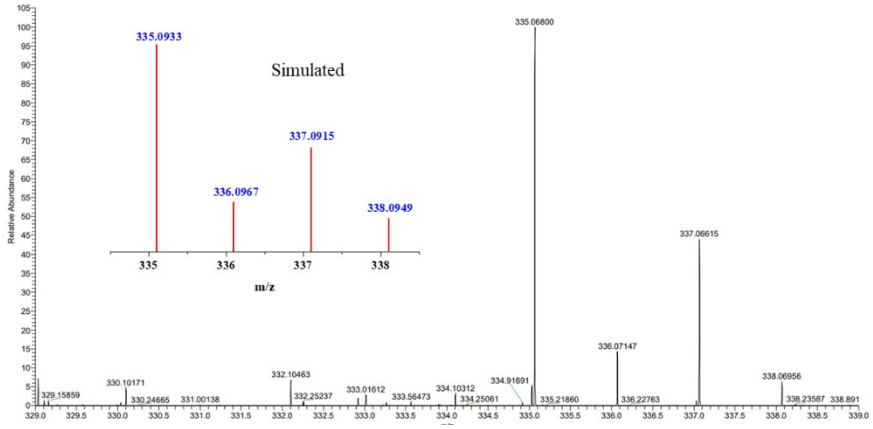

Fig. S20 The measured and simulated high resolution mass spectrum peak of the fragment of $[Cu(dmabpy)(OH)\text{-}CH_3]^+$ from complex **1** after consecutive CV test.

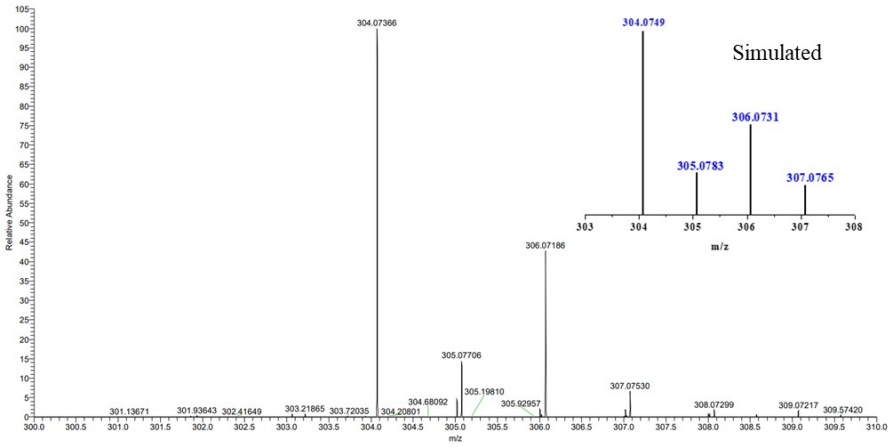

Fig. **S21** The measured and simulated high resolution mass spectrum peak of the fragment of $[Cu(mabpy)\text{-}H^+]^+$ from complex 2 after consecutive CV test.

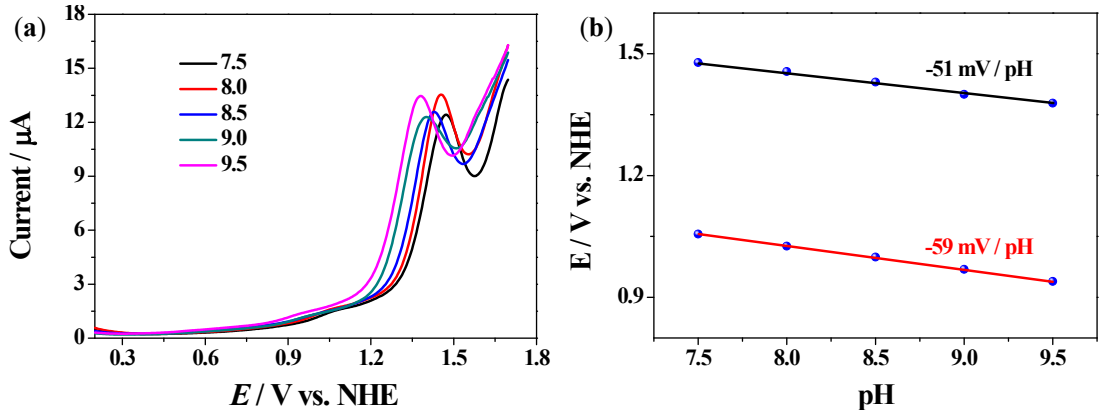

Fig. S22 DPV curves of 1 mM of complex **1** in 0.1 M PBS at various pH (a) and Pourbaix diagram of complex **1** in 0.1 M PBS pH range of 7.5–9.5 (b).

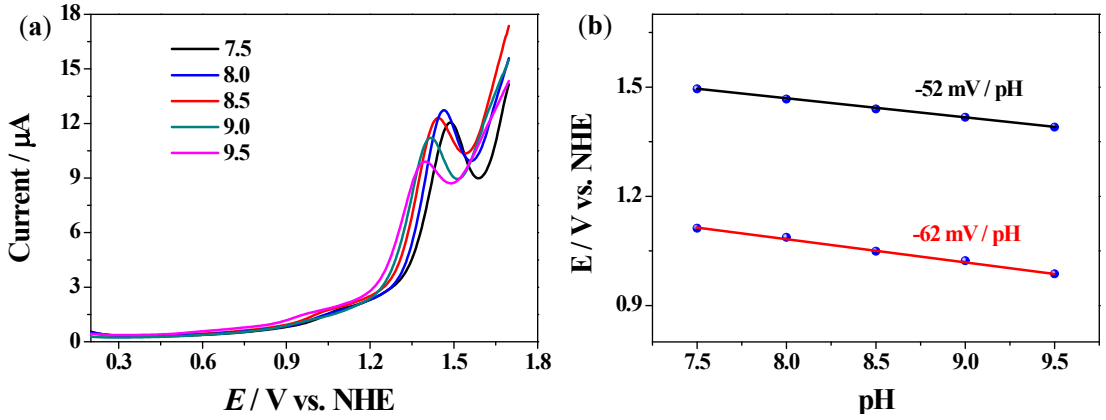

Fig. S23 DPV curves of 1 mM of complex **2** in 0.1 M PBS at various pH (a) and Pourbaix diagram of complex **2** in 0.1 M PBS pH range of 7.5–9.5 (b).

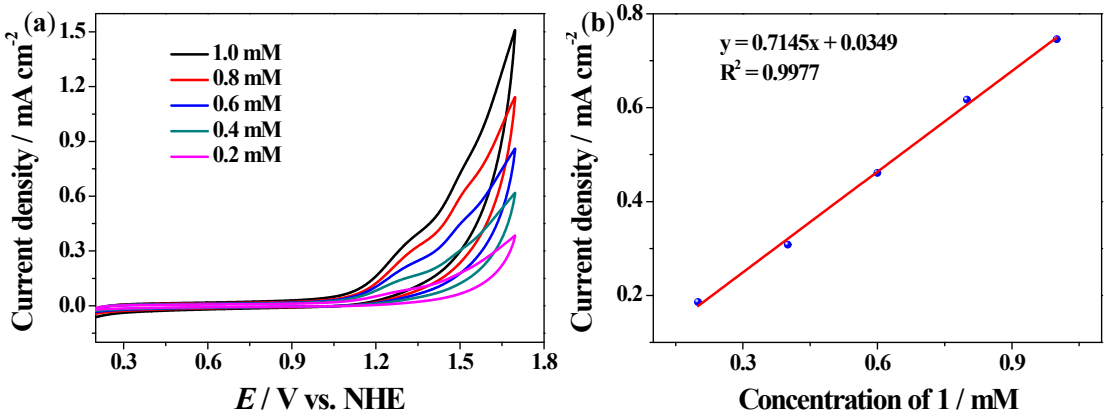

Fig. S24 CV of various concentration of **1** at pH 9.0 with scan rate of 100 mV s^{-1} (a) and the dependence of catalytic current density at 1.50 V vs. NHE on the concentration of **1** (b).

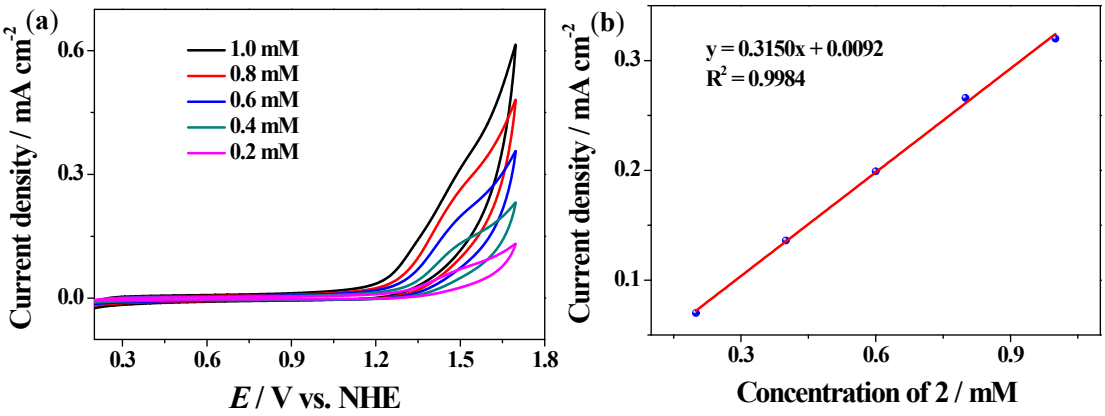

Fig. S25 CV of various concentration of **2** at pH 9.0 with scan rate of 100 mV s^{-1} (a) and the dependence of catalytic current density at 1.50 V vs. NHE on the concentration of **2** (b).

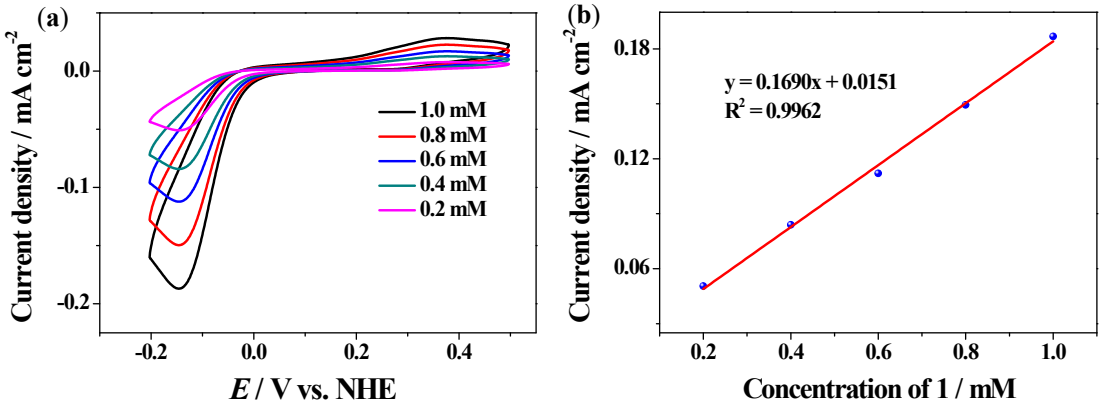

Fig. S26 Cyclic voltammograms of 1.0 mM of **1** with various concentration (a) and dependence of reduction wave current density of the Cu^{I}/Cu^{II} couple of **1** on its concentration (b).

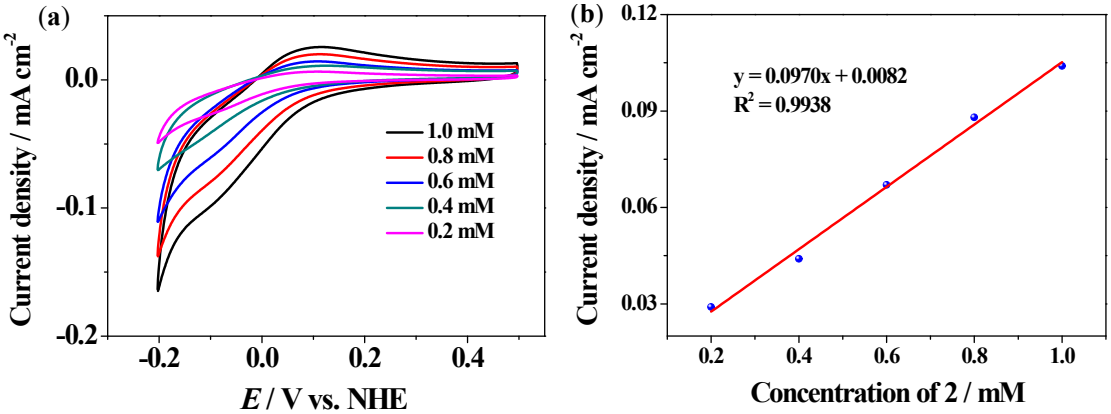

Fig. S27 Cyclic voltammograms of 1.0 mM of **2** with various concentration (a) and dependence of reduction wave current density of the Cu^{I}/Cu^{II} couple of **2** on its concentration (b).

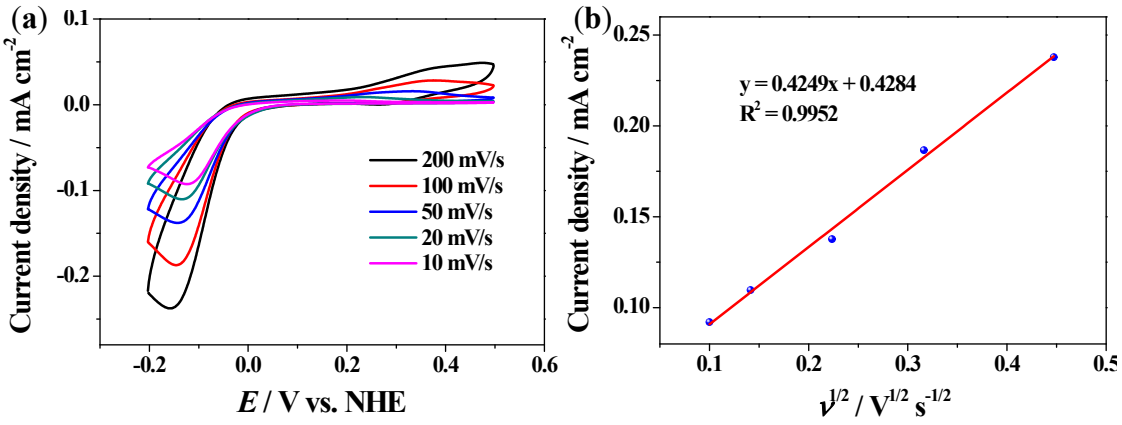

Fig. S28 CV of 1.0 mM of **1** with various scan rate (a) and dependence of reduction wave current density of the Cu^{I}/Cu^{II} couple of **1** on the square root of scan rates (b).

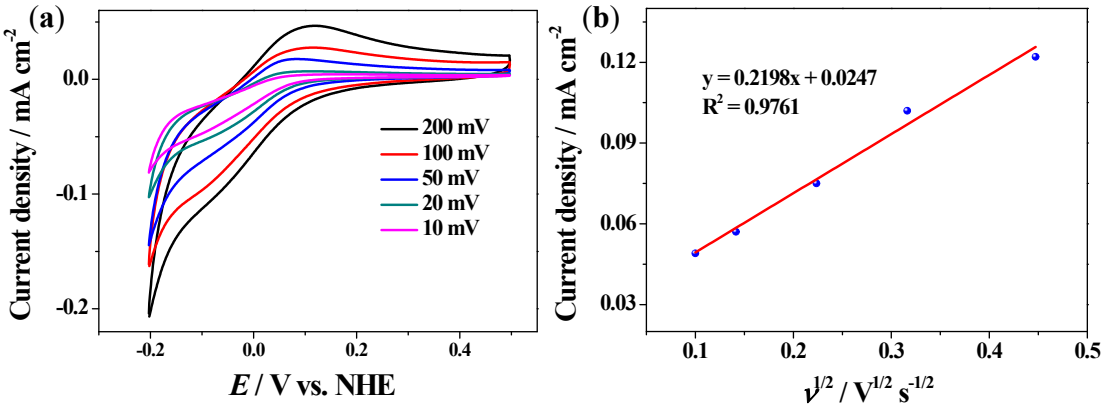

Fig. S29 CV of 1.0 mM of **2** with various scan rate (a) and dependence of reduction wave current density of the Cu^{I}/Cu^{II} couple of **2** on the square root of scan rates (b).

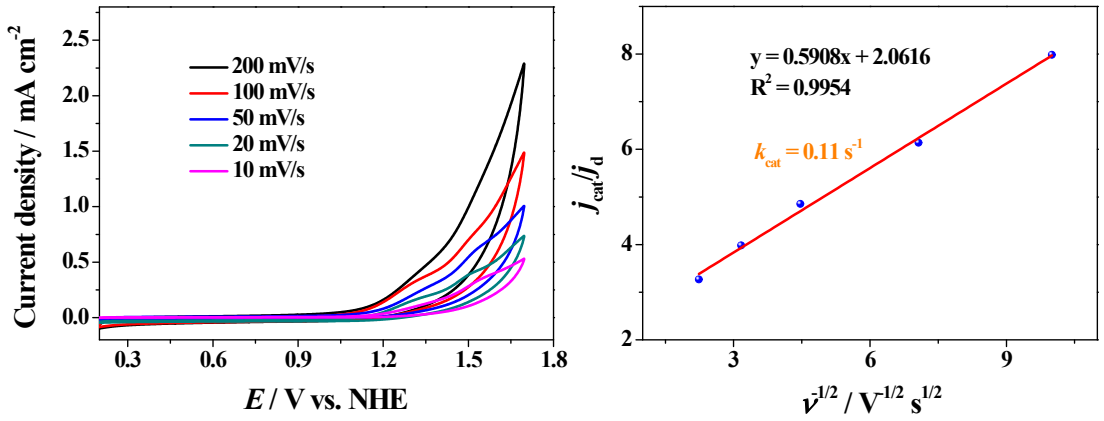

Fig. S30 CV of 1.0 mM of **1** in 0.1 M PBS with scan rate varying from 10 to 200 mV s^{-1} (a) and plots of the ratio of j_{cat} to j_d of **1** versus the reciprocal of the square root of the scan rate (b).

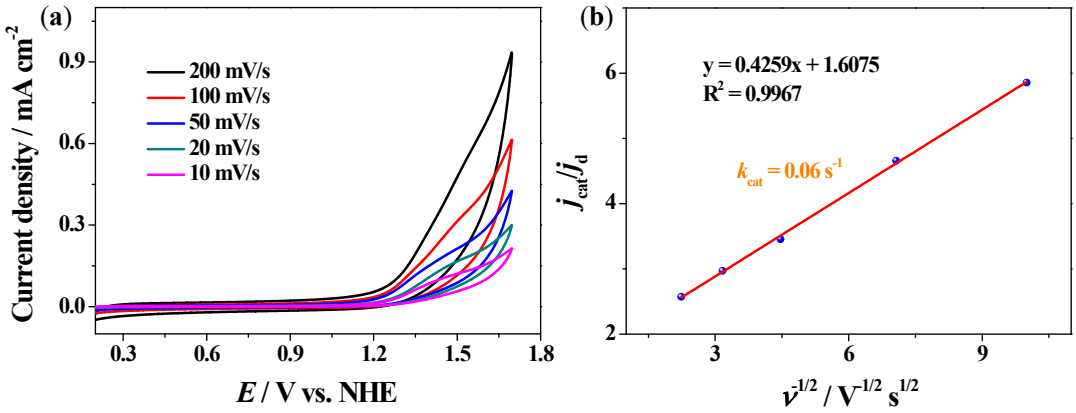

Fig. S31 CV of 1.0 mM of **2** in 0.1 M PBS with scan rate varying from 10 to 200 mV s^{-1} (a) and plots of the ratio of j_{cat} to j_d of **2** versus the reciprocal of the square root of the scan rate (b).

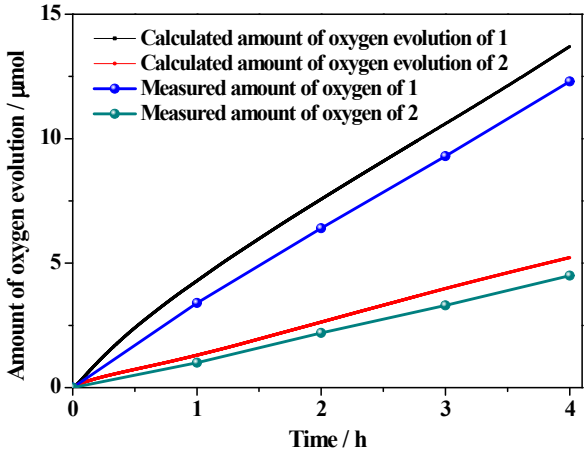

Fig. S32 Faradaic efficiency of O_2 evolution for **1** (a) and **2** (b) under 4 h of electrolysis at 1.50 V vs. NHE in 0.1 M PBS at pH 9.0.

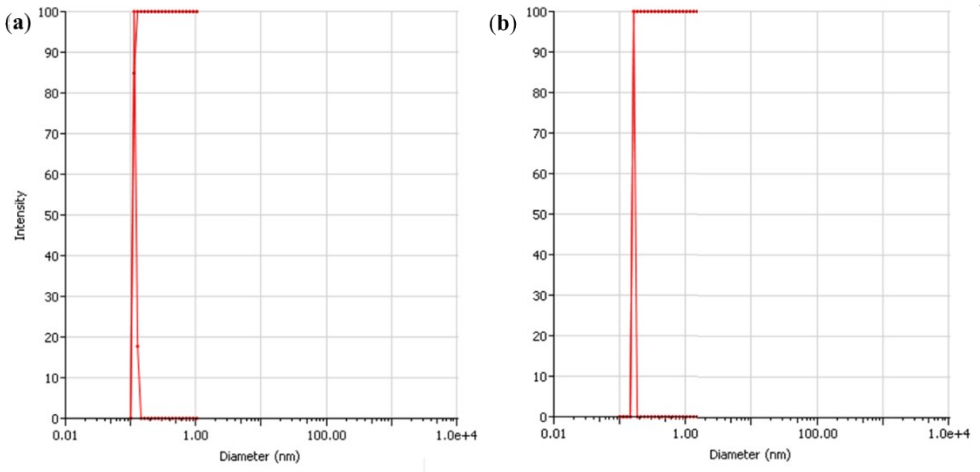

Fig. S33 The dynamic light scattering (DLS) measurement of the solutions after CPE experiment of complex **1** (a) and **2** (b).

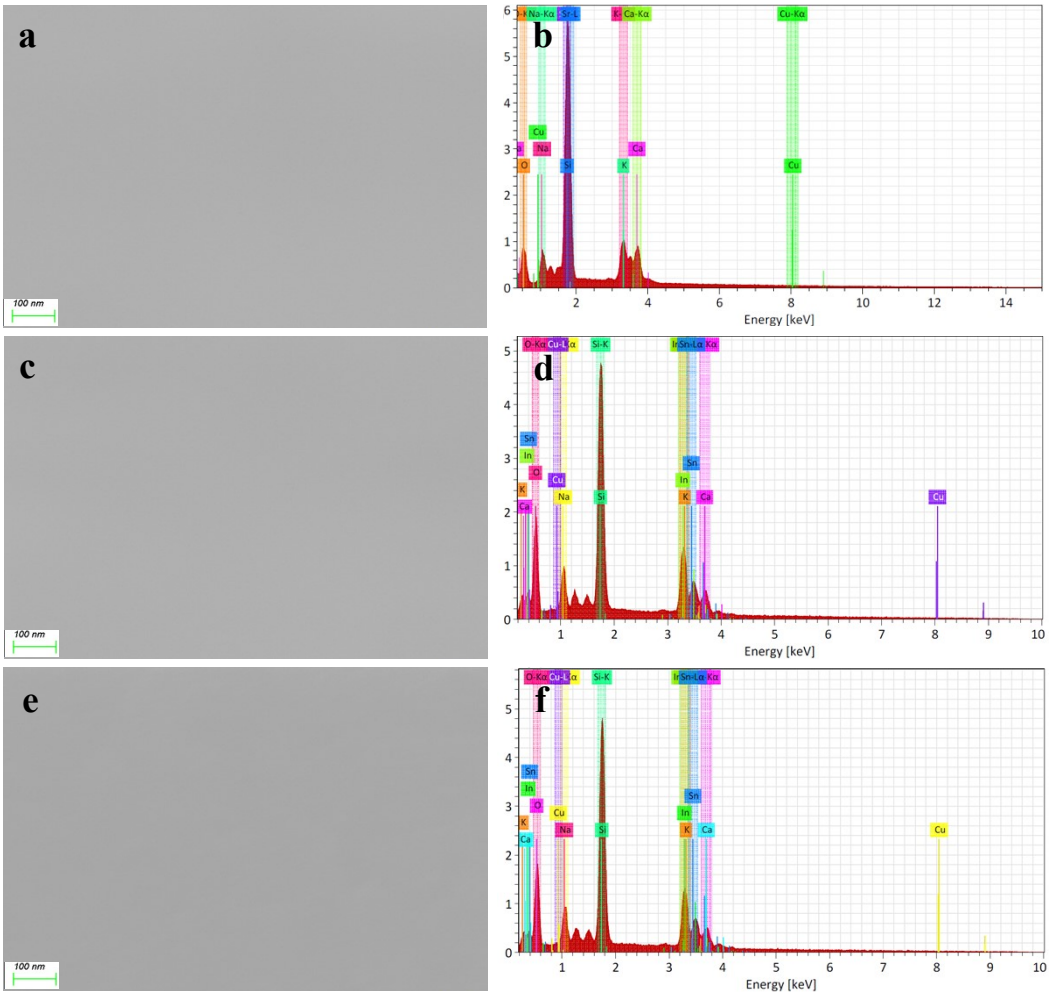

Fig. S34 SEM images and EDX analysis result of the surface of ITO electrode before (a and b) and after 4 h CPE experiments of **1** (c and d) and **2** (e and f) in 0.1 M PBS at pH 9.0.

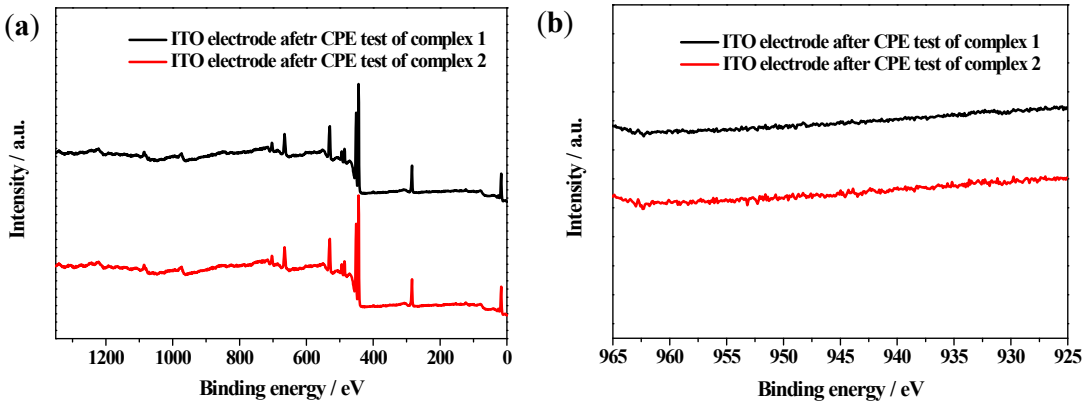

Fig. S35 Full scan of XPS spectra of ITO electrode before and after CPE test with complex **1** and **2** as catalyst (a). XPS spectra of Cu element on ITO electrode before and after CPE test with complex **1** and **2** (b).

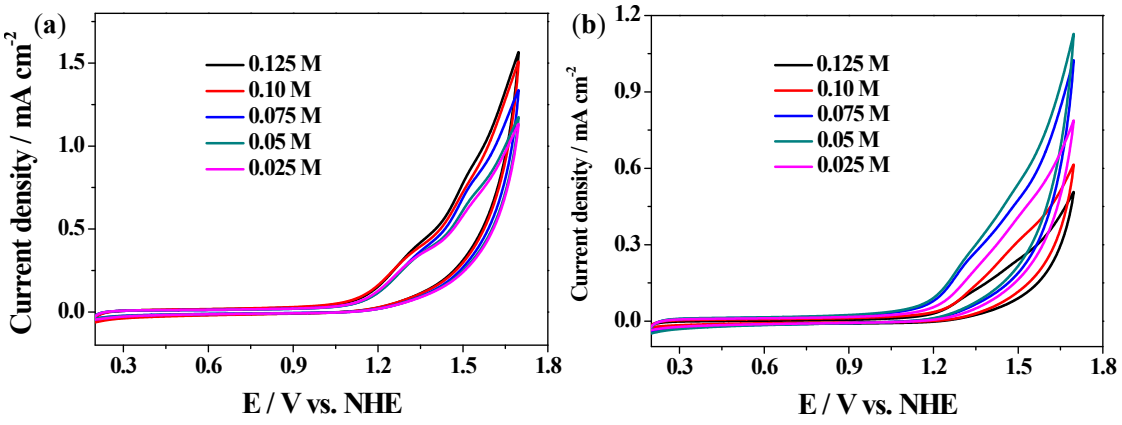

Fig. S36 CV of 1.0 mM of **1** (a) and **2** (b) in pH 9.0 PBS with different concentration.

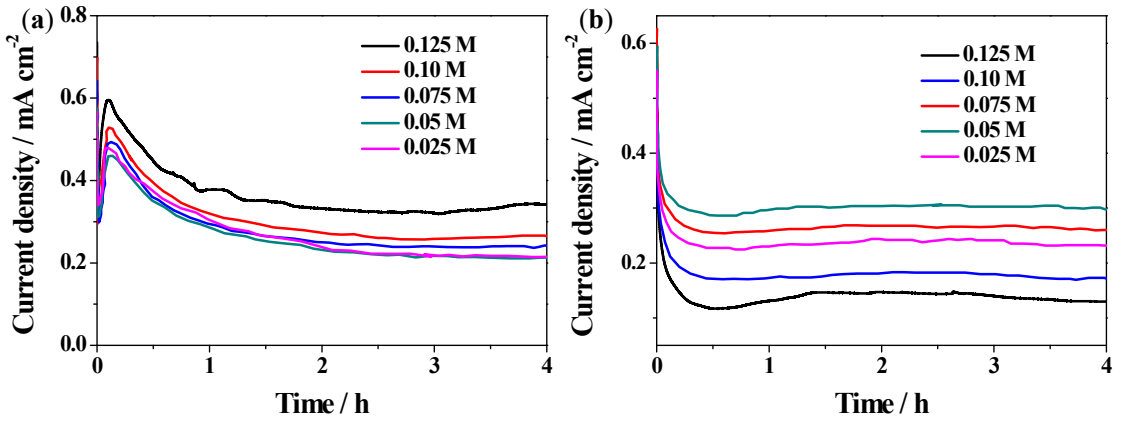

Fig. S37 Catalytic current obtained at the controlled potential electrolysis in the presence of 1 mM complex **1** and **2** using an FTO electrode (1 cm × 2 cm, 1 cm^2 immersed in electrolyte) in PBS (various concentration, pH 9.0) at 1.50 V vs. NHE.

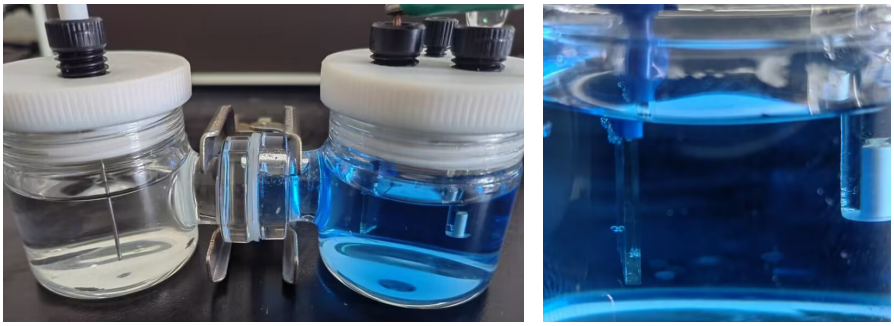

Fig. S38 The photograph of the H-shape electrolyte cell and the oxygen generated on the surface of ITO electrode during the CPE test of complex **1**.

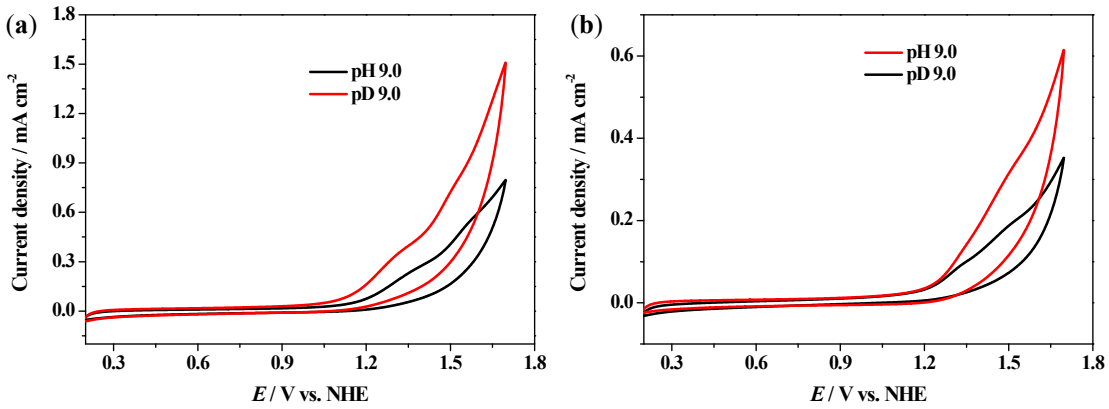

Fig. S39 CV complex **1** (a) and **2** (b) in H_2O or D_2O PBS at pH 9.0, scan rate of 100 mV s^{-1}.

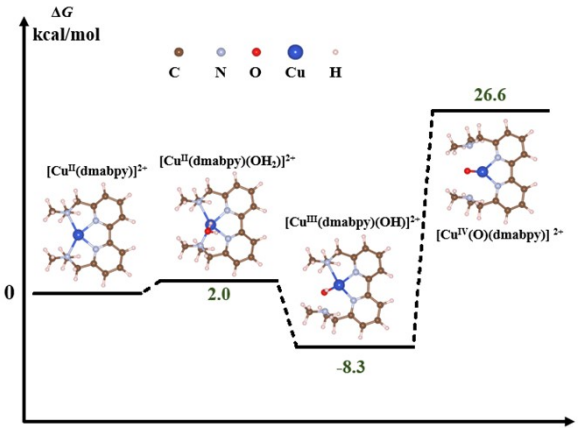

Fig. S40 Relative free energy (ΔG) diagram of the oxidation process of complex **1**. DFT calculations were conducted through the Vienna ab initio Simulation Package (VASP) with the projector augment wave method. Generalized gradient approximation of the Perdew-Burke-Ernzerhof (PBE) functional was used as the exchange-correlation functional. The Brillouin zone was sampled with 2 × 2 × 1 K points for surface calculation. The cutoff energy was set as 500 eV, and structure relaxation was performed until the convergence criteria of energy and force reached 1 × 10^{-5} eV and 0.02 eV $Å^{-1}$, respectively. A vacuum layer of 15 Å was constructed to eliminate interactions between periodic structures of surface models. The van der Waals (vdW) interaction was amended by the zero damping DFT-D3 method of Grimme The Gibbs free energy was calculated as ΔG = ΔE + ΔEZPE −TΔS, where the ΔE, ΔEZPE, and ΔS are electronic energy, zero-point energy, and entropy difference between products and reactants. The zero-point energies of isolated and absorbed intermediate products were calculated from the frequency analysis. The vibrational frequencies and entropies of molecules in the gas phase were obtained from the National Institute of Standards and Technology (NIST) database.

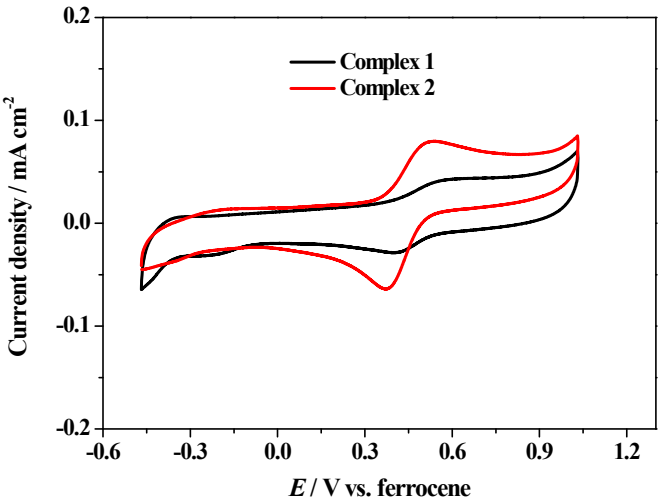

Fig. S41 The CV curves of complex **1** and **2** in anhydrous acetonitrile (0.1 M of tetrabutyl ammonium hexafluorophosphate is used as electrolyte) at 100 mV/s.

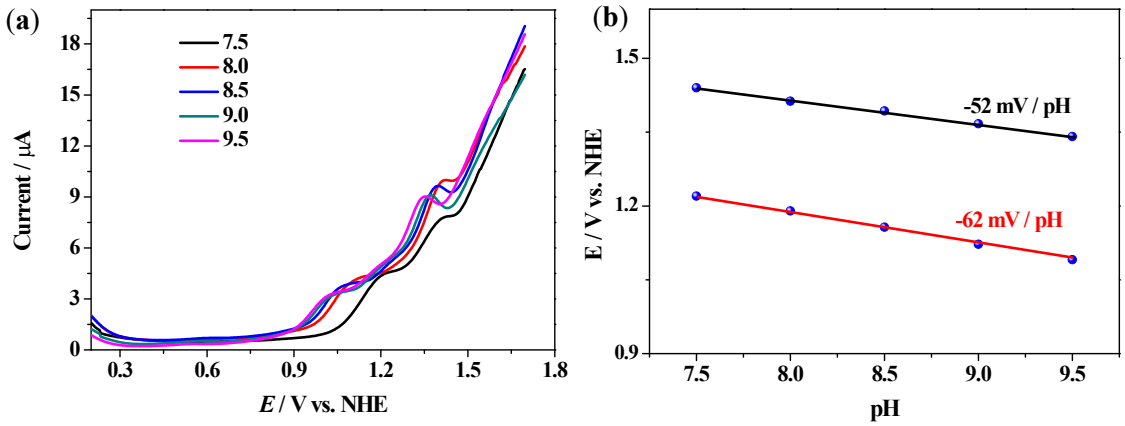

Fig. S42 DPV curves (a) and Pourbaix diagram (b) of 1 mM of **3** in 0.1 M PBS at various pH.

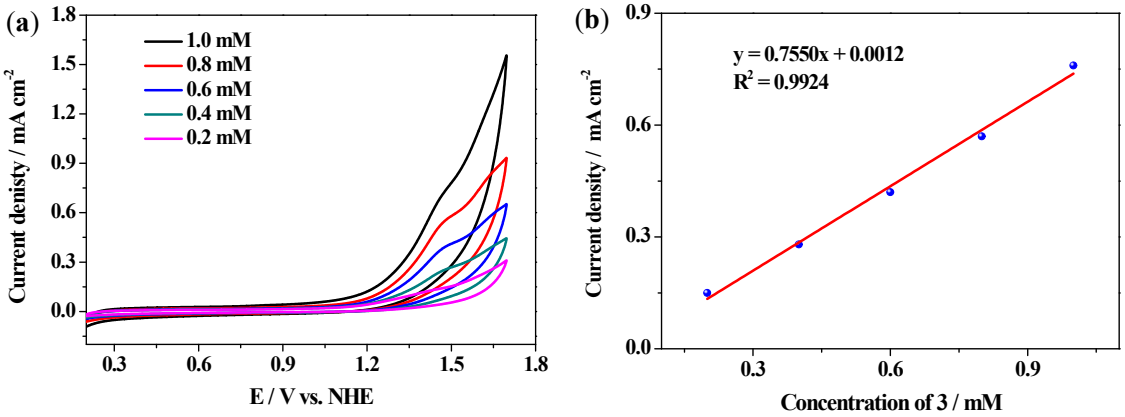

Fig. S43 CV of various concentration of **3** at pH 9.0 with scan rate of 100 mV s^{-1} (a) and the dependence of catalytic current density at 1.48 V vs. NHE on the concentration of **3** (b).

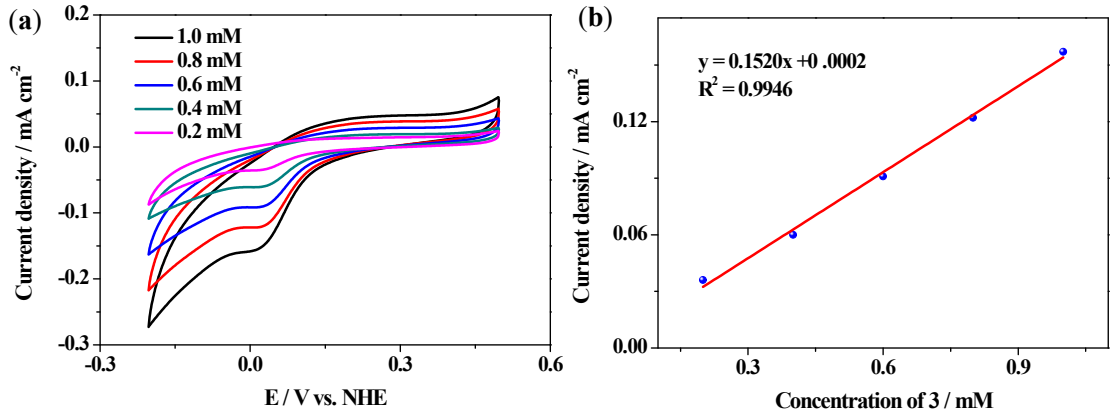

Fig. S44 Cyclic voltammograms of 1.0 mM of **3** with various concentration (a) and dependence of anodic wave current density of the Cu^{I}/Cu^{II} couple of **3** on its concentration (b).

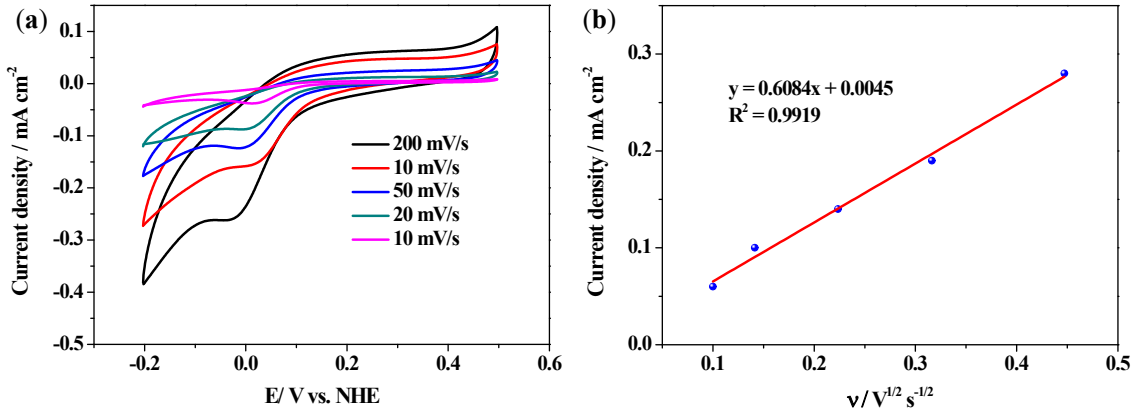

Fig. S45 CV of 1.0 mM of **3** with various scan rate (a) and dependence of reduction wave current density of the Cu^{I}/Cu^{II} couple of **3** on the square root of scan rates (b).

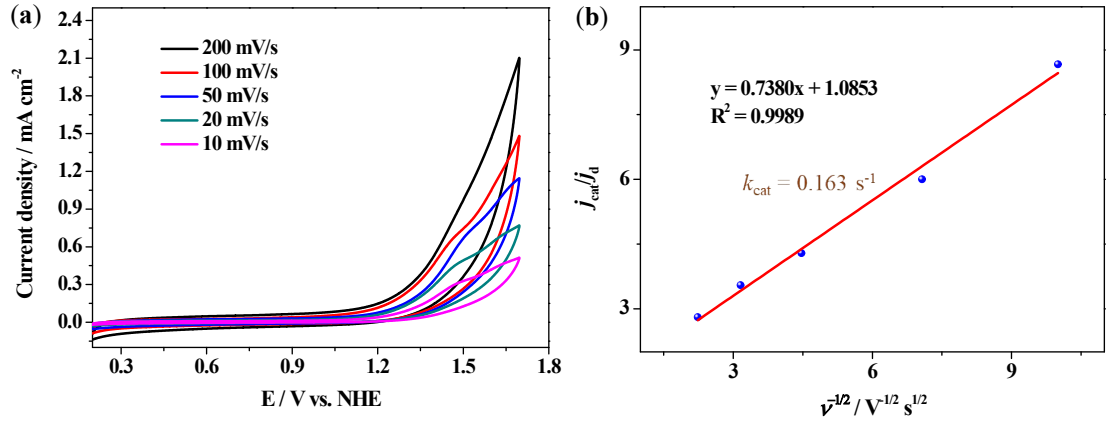

Fig. S46 CV of 1.0 mM of **3** in 0.1 M PBS with scan rate varying from 10 to 200 mV s^{-1} (a) and plots of the ratio of j_{cat} to j_d of **3** versus the reciprocal of the square root of the scan rate (b).

Table S4 Overpotential of homogeneous electrochemical water oxidation catalyzed by some reported Cu-based water oxidation catalysts

Catalyst [a]	pH	η/mV [b]	Ref.
(bpy)$Cu(OH)_2$	13.1	750	S7
[(Me_2TMPA)(μ-OH)$Cu]_2^{2+}$	12.5	636	S8
$[Cu^{II}(L)]^{2+}$	12.0	830	S9
$[L_{Glu}\text{-}Cu)_4]$	12.0	880	S10
$[L_{Gly}\text{-}Cu)_4]$	12.0	880	S10
$[(L4)Cu]^{2-}$	11.6	754	S11
$[Cu(N_2Py_3)]^{2+}$	12.0	831	S12
$[(opba)Cu]^{2-}$	10.8	636	S13
[Cu(Me_2oxpn)$Cu(OH)_2$]	10.4	636	S14
$[L\text{-}Cu\text{-}CO_3H]^-$	10.0	650	S15
$[CuL_2]^{2+}$	9.20	602	S16
$[Cu_2(BPMAN)(\mu\text{-}OH)]^{3+}$	7.0	800	S17
$CuMe_4$cyclam	7.0	880	S18
$[Cu(I)(C2)]^+$	6.5	674	S19
$Cu_2(BEE)_2$	9.35	470	S20
CuPcTS	9.5	570	S21
[(**L1**)$Cu(OH_2)]^{2+}$	9.0	730	S22
[(**L2**)$Cu(OH_2)]^{2+}$	9.0	330	S22
Complex **1**	9.0	600	This work

[a] The structures of the catalysts listed in this table are given below. [b] η = onset overpotential obtained from CV test (vs. NHE).

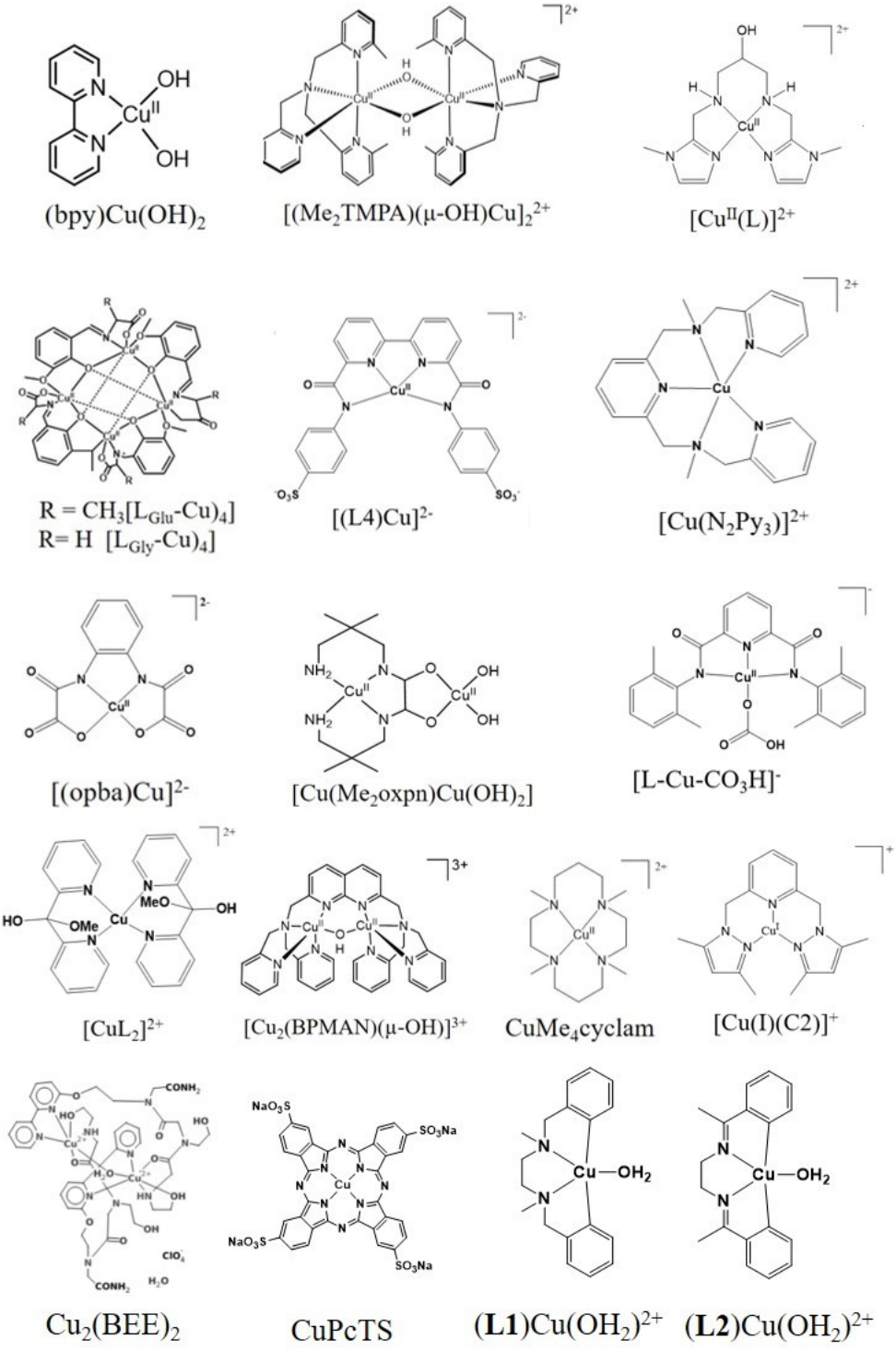

Reference

S1 G. Kresse and D. Joubert, *Phys. Rev. B*, 1999, **59**, 1758–1775.

S2 P. E. Blöchl, *Phys. Rev. B*, 1994, **50**, 17953–17979.

S3 J. P. Perdew, K. Burke and M. Ernzerhof, *Phys. Rev. Lett.*, 1996, **77**, 3865–3868.

S4 S. Grimme, S. Ehrlich and L. Goerigk, *J. Comput. Chem.*, 2011, **32**, 1456–1465.

S5 J. K. Nørskov, J. Rossmeisl, A. Logadottir, L. Lindqvist, J.R. Kitchin, T. Bligaard and H. Jónsson, *J. Phys. Chem. B*, 2004, **108**, 17886–17892.

S6 J. K. Nørskov, T. Bligaard, A. Logadottir, J. R. Kitchin, J. G. Chen, S. Pandelov and U. Stimming, *J. Electrochem. Soc.*, 2005, 152.

S7 S. M. Barnett, K. I. Goldberg and J. M. Mayer, *Nat. Chem*., 2012, **4**, 498−502.

S8 S. J. Koepke, K. M. Light, P. E. VanNatta, K. M. Wiley and M. T. Kieber-Emmons, *J. Am. Chem. Soc*., 2017, **139**, 8586−8600.

S9 S. Nestke, E. Ronge and I. Siewert. *Dalton Trans*., 2018, **47**, 10737-10741.

S10 X. Jiang, J. Li, B. Yang, X.-Z. Wei, B.-W. Dong, Y. Kao, M.-Y. Huang, C.-H. Tung and L.-Z. Wu, *Angew. Chem. Int. Ed.*, 2018, **57**, 7850–7854.

S11 M. Gil-Sepulcre, P. Garrido-Barros, J. Oldengott, I. Funes-Ardoiz, R. Bofill, X. Sala, J. Benet-Buchholz and A. Llobet, *Angew. Chem. Int. Ed.*, 2021, **60**, 18639−18644.

S12 Z. Xu, Z. Zheng, Q. Chen, J. Wang, K. Yu, X. Xia, J. Shen and Q. Zhang, *Dalton Trans.*, 2021, **50**, 10888–10895.

S13 L.-Z. Fu, T. Fang, L.-L. Zhou and S.-Z. Zhan, *RSC Adv*., 2014, **4**, 53674−53680.

S14 L.-L. Zhou, T. Fang, J.-P. Cao, Z.-H. Zhu, X.-T. Su and S.-Z. Zhan, *J. Power Sources.*, 2015, **273**, 298−304.

S15 F. Chen, N. Wang. H. Lei, D. Guo, H. Liu, Z. Zhang, W. Zhang, W. Lai and R. Cao, *Inorg. Chem.*, 2017, **56**, 13368–13375.

S16 N. N. Shi , W. J. Xie , D. M. Zhang, Y. H. Fan, L. S. Cui and M. Wang. *J. Electroanal. Chem.*, 2021, **886**, 115106.

S17 X.-J. Su, M. Gao, L. Jiao, R.-Z. Liao, P. E. M. Siegbahn, J.-P. Cheng and M.-T. Zhang, *Angew. Chem. Int. Ed*., 2015, **54**, 4909−4914.

S18 A. Prevedello, I. Bazzan, N. D. Carbonare, A. Giuliani, S. Bhardwaj, C. Africh, C. Cepek, R. Argazzi, M. Bonchio, S. Caramori, M. Robert and A. Sartorel, *Chem. Asian J*., 2016, **11**, 1281−1287.

S19 T. Makhado, B. Das, R. J. Kriek, H. C. M. Voslooa and A. J. Swarts, *Sustainable Energy Fuels.*, 2021, **5**, 2771-2780.

S20 G. Ruan, P. Ghosh, N. Fridman and G. Maayan, *J. Am. Chem. Soc.*, 2021, **143**, 28, 10614–10623.

S21 R. Terao, T. Nakazono, A. R. Parent and K. Sakai, *ChemPlusChem*, 2016, **81**, 1064−1067.

S22 J. Shen, M. Wang, J. Gao, H. Han, H. Liu and L. Sun, *ChemSusChem*, 2017, **10**, 4581–4588.